HOKKAIDO UNIVERSITY

Title	Magnetic properties and structural transitions of fluorite-related rare earth osmates Ln3Os07 (Ln=Pr, Tb)
Author(s)	Hinatsu, Yukio; Doi, Yoshihiro
Citation	Journal of Solid State Chemistry, 198, 176-185 https://doi.org/10.1016/j.jssc.2012.09.039
Issue Date	2013-02
Doc URL	https://hdl.handle.net/2115/52119
Type	journal article
File Information	JSSC198_176-185.pdf

Hokkaido University Collection of Scholarly and Academic Papers : HUSCAP

Magnetic Properties and Structural Transitions of Fluorite-Related Rare Earth Osmates Ln_3OsO_7 (Ln = Pr, Tb)

Yukio Hinatsu* and Yoshihiro Doi

Division of Chemistry, Graduate School of Science, Hokkaido University, Sapporo 060-0810, Japan

*tel/fax: +81-11-706-2702

email:hinatsu@sci.hokudai.ac.jp

Abstract

Ternary rare-earth osmates Ln_3OsO_7 (*Ln* = Pr, Tb) have been prepared. They crystallize in an orthorhombic superstructure of cubic fluorite with space group *Cmcm*. Both of these compounds undergo a structural phase transition at 130 K (*Ln* = Pr) and 580 K (*Ln* = Tb). These compounds show complex magnetic behavior at low temperatures. Pr_3OsO_7 exhibits magnetic transitions at 8 and 73 K, and Tb_3OsO_7 magnetically orders at 8 and 60 K. The Os moments become one-dimensionally ordered, and when the temperature is furthermore decreased, provokes the ordering in the Ln^{3+} sublattice that simultaneously becomes three-dimensionally ordered with the Os sublattice.

1. Introduction

Ternary metal oxides of general formula Ln_3MO_7 (*Ln* is a rare earth element; *M* is a pentavalent transition element such as Nb, Mo, Ru, Sb, Ta, Re, Os, or Ir) have been intensively studied, because of their one-dimensional structural features and possible magnetic properties. They have an ordered, defect-fluorite structure. The relationship to the fluorite structure is as follows. The fluorite unit cell for oxides has the composition $M^{4+}{}_4O_8$. If the four tetravalent metal ions are replaced by three trivalent ions (*Ln*) and one pentavalent ion (*M*), one oxide vacancy is formed per fluorite cell. Due to significant differences in radii between the Ln^{3+} and M^{5+} ions, cation ordering occurs on the metal sites and the oxide-vacancy orders on the anion sites. The M^{5+} ion is coordinated with six oxygen ions, forming a MO_6 octahedron. These octahedra share corners forming one-dimensional chains which are oriented along the *c*-axis. One-third of Ln ions are coordinated by eight oxygen ions and the distorted LnO_8 cubes also form a one-dimensional chain through edge-sharing. Many studies have been performed [1-28], especially for the magnetic properties of compounds containing Ru^{5+} ion at the *M*-site because of its largest possible spin ($S = 3/2$) [5-12].

Another topic for Ln_3MO_7 compounds is that detailed magnetic and thermal investigations on the ruthenium-, iridium- and osmium-containing members of the Ln_3MO_7 family show low-temperature structural phase transitions [8-10, 12, 13, 18, 22, 25, 26, 29-34].

We have paid our attention on the *M* = Os compounds. IJdo et al. first reported the preparation, structures and magnetic properties of polycrystalline samples of Ln_3OsO_7 (*Ln* = Pr, Nd, Sm) [17]. These compounds crystallized in an orthorhombic phase with space group *Cmcm* from their powder X-ray diffraction measurements, and *Ln* = Nd and Sm compounds exhibited complex magnetic behavior at

low temperatures. Later, Greedan et al. prepared La_3OsO_7 and reported the presence of the evidence for long-range antiferromagnetic ordering at 45 K [11]. Recently zur Loye's research group prepared single crystals of Ln_3OsO_7 (*Ln* = Sm, Eu, Gd) and performed their X-ray diffraction measurements [18]. They observed that these compounds undergo a structural phase transition from space group *Cmcm* to $P2_1nb$ and exhibit complex magnetic behavior below 50 K.

In this study, we prepared Ln_3OsO_7 (*Ln* = Pr, Tb) without using oxygen donor reactants. Through their magnetic susceptibility, specific heat and differential scanning calorimetry (DSC) measurements, we observed an antiferromagnetic transition at 73 K (*Ln* = Pr) and 60 K (*Ln* = Tb), and a phase transition at 130 K (*Ln* = Pr) and 580 K (*Ln* = Tb). In this paper, the preparation, structures, and magnetic properties of these compounds will be presented.

2. Experimental

2.1. Sample preparation

Rare earth oxides Pr_6O_{11} (99.99 %, Shin-etsu Chemical) and Tb_4O_7 (99.9 %, Shin-etsu Chemical) and an osmium oxide OsO_2 (99.99 %, Premion from Alfa Aesar) were used as starting materials. Pr_3OsO_7 and Tb_3OsO_7 were prepared in a closed system:

$$3/4\ Pr_2O_3 + 1/4\ Pr_6O_{11} + OsO_2 \rightarrow Pr_3OsO_7,$$

$$1/2\ Tb_2O_3 + 1/2\ Tb_4O_7 + OsO_2 \rightarrow Tb_3OsO_7.$$

For the preparation of sesquioxides Pr_2O_3 and Tb_2O_3, the Pr_6O_{11} and Tb_4O_7 were reduced in a flowing H_2 atmosphere at 900 °C for a day. These starting materials were weighed in an appropriate metal ratio and were ground in an agate mortar. The mixtures were pressed into pellets and then sealed in an

evacuated quartz tube. They were heated at 950 °C for 5 h, and then cooled down to room temperature.

2.2. X-ray diffraction analysis

Powder X-ray diffraction profiles were measured using a Rigaku Multi-Flex diffractometer with Cu-*Kα* radiation (λ = 1.5406 Å) equipped with a curved graphite monochromator. The data were collected by step-scanning in the angle range of $10° \leq 2\theta \leq 120°$ at a 2θ step-size of 0.02°. For Tb_3OsO_7, the temperature dependence of the X-ray diffraction profiles ($15° \leq 2\theta \leq 120°$) was obtained in the temperature range from 373 to 723 K.

The X-ray diffraction data were analyzed by the Rietveld technique, using the programs RIETAN-FP [35], and the crystal structure was drawn by using the VESTA program [36].

2.3. Magnetic susceptibility measurements

The temperature-dependence of the magnetic susceptibility was measured in an applied field of 0.1 T over the temperature range of $1.8\ \text{K} \leq T \leq 400\ \text{K}$, using a SQUID magnetometer (Quantum Design, MPMS5S). The susceptibility measurements were performed under both zero-field-cooled (ZFC) and field-cooled (FC) conditions. The former was measured upon heating the sample to 400 K under the applied magnetic field of 0.1 T after zero-field cooling to 1.8 K. The latter was measured upon cooling the sample from 400 to 1.8 K at 0.1 T. For Tb_3OsO_7, the temperature dependence of its susceptibility was measured under the applied magnetic field of 0.01 T.

The remnant magnetization measurements were also performed. The samples were cooled to 1.8 K in a zero magnetic field. The magnetic field was applied up to 5 T and then reduced to zero. The magnetization measurements were performed in the temperature range from 1.8 K to room temperature.

The field dependence of the magnetization was measured for Tb_3OsO_7 at several temperatures (5,

20, 50 K) by changing the magnetic field strength in the range between -5 T and 5 T.

2.4. Specific heat measurements

Specific heat measurements were performed using a relaxation technique by a commercial heat capacity measuring system (Quantum Design, PPMS) in the temperature range of 1.8-400 K. The sintered sample in the form of a pellet was mounted on a thin alumina plate with Apiezon for better thermal contact.

2.5. ac magnetic susceptibility measurements

The ac magnetic susceptibility measurements were performed for Tb_3OsO_7 with the same measurement system (Quantum Design, PPMS) in the temperature range between 1.8 and 100 K. The temperature dependence of the ac susceptibilities was measured at 10, 100, 1,000, and 10,000 Hz. The samples were first cooled in a zero magnetic field and then an ac field was applied up to 0.0005 T.

2.6. Differential scanning calorimetry (DSC) measurements

The DSC measurements were carried out under flowing Ar gas atmosphere over the temperature range 350-700 K using DSC 200 (Seiko, Japan). The heating rate was 5 K/min.

3. Results and discussion

3.1. Preparation and crystal structure

Two rare earth osmates Pr_3OsO_7 and Tb_3OsO_7 were isolated from the reaction of a mixture of Pr_2O_3 (Tb_2O_3), Pr_6O_{11} (Tb_4O_7) and OsO_2 in a closed system, without using oxygen donor reactants. Concerning the preparation of osmium-containing oxides, Plaisier and IJdo reported that it is difficult to control the oxidation state of osmium in oxides by using oxygen donor reactants [17]. In the present

study, we used OsO_2 instead of Os metal as a starting material, which considerably reduces the formation of volatile osmium tetroxide OsO_4. In addition, for the case of preparing Pr_3OsO_7 and Tb_3OsO_7, we need not use oxygen donors such as Ag_2O and $KClO_3$, because Pr_6O_{11} and Tb_4O_7 are available.

Figure 1 (a) shows the powder X-ray diffraction profile for Pr_3OsO_7 at room temperature. This diffraction pattern is similar to that for the fluorite structure and all reflections appear to be consistent with the C-centered condition, $h + k = 2n$. A variety of space groups such as *Pnma*, *Cmcm*, $P2_12_12_1$, $C222_1$, $P2/n$ and $P2_1nb$ have been proposed for the Ln_3MO_7. The C-centering extinction condition ruled out space groups such as *Pnma*, $P2_12_12_1$, $P2/n$ and $P2_1nb$. Some extra reflection peaks which should be observed with space group $C222_1$ (for example, the peak at $2\theta \sim 20.5°$ corresponding to the 2 0 1 reflection) were not observed in the X-ray diffraction profile. This fact shows that the $C222_1$ was also ruled out from the space group for Pr_3OsO_7. We performed refinements of the crystal structure with the space group *Cmcm*. All the reflections observed could be successfully indexed. Table 1 lists the crystallographic data for Pr_3OsO_7, and Fig. 2 illustrates the crystal structure of Pr_3OsO_7. The OsO_6 octahedra are corner-linked through the O(3) atoms, and they form one-dimensional chains along the c-axis. One-third of the Pr atoms are in eight-fold oxygen coordination, forming distorted cubes $Pr(1)O_8$. These $Pr(1)O_8$ cubes are aligned one-dimensionally by edge sharing along the c-axis, which alternate with the parallel zigzag chains of Os octahedra, forming slabs parallel to the b-c plane. The remaining two-thirds of Pr(2) ions are in seven coordination and lie between the slabs of the $Pr(1)O_8$ and the OsO_6 polyhedra.

Figure 1 (b) shows the powder X-ray diffraction profile for Tb_3OsO_7 measured at room

temperature. If we assume the same space group with that for Pr_3OsO_7, some reflection peaks (for example at 2θ = 28.9°, 33.3°, 48.2°, and 56.9°) cannot be explained from the extinction condition. As will be described later, Pr_3OsO_7 and Tb_3OsO_7 undergo a crystallographic phase transition at 130 and 580 K, respectively. Therefore, the structure of Tb_3OsO_7 at room temperature should be the one at low temperature phase.

Figure 3 shows the X-ray diffraction profiles of Tb_3OsO_7 measured at various temperatures. We performed the Rietveld analysis for the X-ray diffraction data above 580 K with space group *Cmcm*. The results show that the refinement for the diffraction data was successful with the space group *Cmcm* and that a very small amount of the pyrochlore $Tb_2Os_2O_7$ was contained in the product. Figure 4 shows the X-ray diffraction profiles of Tb_3OsO_7 measured at 673 K. The crystallographic data for Tb_3OsO_7 at 673 K are also listed in Table 1. The Os-O(3)-Os angle is 157.0° for Pr_3OsO_7 and 149.3° for Tb_3OsO_7. This increased buckling of the Os-O(3)-Os angle with decreasing the size of the Ln ion is due to the shortening of the *c*-axis, which is observed for other Ln_3MO_7 compounds.

With decreasing temperature, some additional diffraction lines which cannot be fitted with *Cmcm* appear (for example at 2θ = 28.9°, 33.3°, 48.2°, and 56.9°, see Fig. 3). We consider that these extra diffraction lines originate from a low-temperature phase.

Gemmill et al. reported that Ln_3OsO_7 (*Ln* = Sm, Eu, Gd) compounds undergo a structural phase transition from space group *Cmcm* to $P2_1nb$ with decreasing temperature [18]. We tried to analyze the X-ray diffraction data measured at room temperature with the $P2_1nb$ model. All the reflections observed could be indexed, as shown in Fig. 5. Figure 6 illustrates the crystal structure of Tb_3OsO_7 at room temperature. The lattice parameters determined for Tb_3OsO_7 are a = 10.5514(22) Å, b = 14.7424(38) Å,

c = 7.3771(18) Å, and V = 1145.19(47) Å^3. These values are smaller than those for Gd_3OsO_7 [18]. The structure transitions from *Cmcm* to *P2$_1$nb* involves a distortion in the trans vertex-sharing OsO_6 chains that causes a doubling of the orthorhombic b-axis and a concomitant reduction in the coordination environment of the Tb cations from 8 to 7. On the other hand, the Os-O distances are not much affected by the structural distortion, and the average Os-O distances is 1.947 Å. In the low-temperature structure of Ln_3OsO_7, the average value of Os-O distance within the OsO_6 octahedra decreases from 1.959 to 1.947 Å when the Ln^{3+} ionic radius decreases from Sm to Tb. Similar trends have been reported for the structures of Ln_3MoO_7 (*Ln* = La ~ Gd) compounds [45].

In order to determine the structural phase transition temperature of Tb_3OsO_7, we performed its DSC measurements in the temperature range between 350 and 700 K. Figure 7 depicts the DSC profile of Tb_3OsO_7 during heating. The endothermic reaction begins at ~ 580 K, showing that the structural phase transition occurs at this temperature.

Figure 8 shows the temperature dependence of the lattice parameters and volume for Tb_3OsO_7 in the temperature range of 373 K ≤ T ≤ 723 K. The lattice parameters were refined with space group *Cmcm* for any temperature. With increasing temperature, the lattice parameter *b* increases monotinically, while clear changes have been observed between 573 and 598 K for the parameters *a*, *c* and volume. These changes correspond to the results by the DSC measurements, i.e., the structural phase transition has occurred at ~ 580 K.

3.2. Magnetic properties

3.2.1. Magnetic properties of Pr_3OsO_7

Figure 9 shows the temperature dependence of the magnetic susceptibility for Pr_3OsO_7. A clear divergence between the ZFC and FC susceptibilities has been observed below 73 K. Below this temperature, the FC susceptibility rapidly increases with decreasing temperature, and reaches a maximum at 28 K. Below 4.7 K, the FC susceptibility turns to increase with decreasing temperature. The ZFC susceptibility also increases with decreasing temperature, but the increment of the ZFC susceptibility against temperature drastically changes at 73 and 22 K. It seems that another magnetic anomaly is observed at 8 K. The inset of Fig. 9 shows the temperature dependence of the $d(\chi_M T)/dT$. A great change has been found at 8 K for both the ZFC and FC susceptibility data.

Figure 10 shows the temperature dependence of the specific heat divided by temperature (C_p/T) for Pr_3OsO_7. Specific heat anomalies have been observed at 130, 73, and 8 K. The anomaly at 130 K indicates the existence of the phase transition at this temperature. The anomaly at 73 K is in accordance with the results by the magnetic susceptibility, i.e., a magnetic transition has occurred at this temperature. The λ-type specific heat anomaly observed at 8 K seems to correspond to the anomaly found in the ZFC and FC susceptibilities at the same temperature, indicating the occurrence of another magnetic transition at this temperature. We consider that the Os moments become one-dimensionally ordered at 73 K, and when the temperature is furthermore decreased, provokes the ordering in the Ln^{3+} sublattice that simultaneously becomes three-dimensionally ordered with the Os sublattice at 8 K. Similar magnetic behavior has been reported for Nd_3OsO_7, i.e., two magnetic anomalies are observed at ~10 and 75 K [17].

Figure 11 depicts the temperature dependence of the reciprocal susceptibility of Pr_3OsO_7, and the Curie-Weiss fitting in the temperature range of 100 and 400 K. The effective magnetic moment of

Pr_3OsO_7 is determined to be 6.37 μ_B. It is generally known that the moment of Pr^{3+} is 3.58 μ_B. Assuming the effective moment of 3.58 μ_B per Pr^{3+}, the effective magnetic moment of Os^{5+} is found to be 1.46 μ_B. Since the spin-orbit coupling cannot be ignored for the $5d^3$ ions, the expected moment of Os^{5+} should be lower than the spin-only value of 3.87 μ_B. Comparable lower effective magnetic moment of Os^{5+} is reported for Nd_3OsO_7 [17]. That is, the contribution of the Os^{5+} ions to the effective magnetic moment of Pr_3OsO_7 is small, which has been observed in some Os-containing compounds [17, 37-42].

The negative Weiss constant of Pr_3OsO_7 (θ = -39.9 K) indicates that the magnetic interaction observed at low temperatures is antiferromagnetic.

3.2.2. Magnetic properties of Tb_3OsO_7

Figure 12 shows the magnetic susceptibility vs temperature curve of Tb_3OsO_7 in the temperature range between 1.8 and 300 K. The ZFC and FC susceptibilities begin to diverse when the temperature is decreased through ca 60 K. At 26 K, the temperature dependence of the ZFC susceptibility shows a steep maximum. On the contrary, the FC susceptibility shows a clear click at the same temperature. When the temperature is furthermore decreased, a clear antiferromagnetic behavior has been observed for both the ZFC and FC susceptibilities at 8 K. A very small anomaly found at 2.4 K in the ZFC susceptibility-temperature curve is due to the antiferromagnetic ordering of an impurity Tb_2O_3 (a starting material) with the C-type structure [43, 44].

Figure 13 shows the temperature dependence of the in-phase and out-of-phase magnetic susceptibility for Tb_3OsO_7 in the temperature range of 1.8-100 K. When the temperature is decreased below 60 K, both the in-phase and the out-of-phase susceptibilities change with the frequency. There

appear two maxima at 8 and 28 K in the in-phase susceptibility vs. temperature curve. The temperature of the maximum ac susceptibilities for Tb_3OsO_7 appears to be independent of the frequency, indicating that the transition is not a transition to a spin-glass state.

Figure 14 shows the temperature dependence of the specific heat (C_p) for Tb_3OsO_7. Two specific heat anomalies have been observed at 2.4 and 8 K. The anomaly at 8 K is in accordance with the results by the magnetic susceptibility, i.e., a magnetic transition has occurred at this temperature. Another anomaly observed at 2.4 K is due to the Tb_2O_3 as an impurity in the sample. From the results of magnetic susceptibility and specific heat measurements, we consider that the Os moments become one-dimensionally ordered at ca 60 K. When the temperature is furthermore decreased, provokes the ordering in the Ln^{3+} sublattice that simultaneously becomes three-dimensionally ordered with the Os sublattice at 8 K.

Figure 15 shows the field dependence of the magnetization of Tb_3OsO_7 measured at 5, 20, and 50 K. Even at 50 K, the magnetization vs the applied magnetic field curve is not linear. It is clear that at 5K, there exists an isothermal magnetization loop. From the large divergence between ZFC and FC magnetic susceptibilities, there exists a ferromagnetic component in the antiferromagnetic moments.

To check the existence of the ferromagnetic moment, the remnant magnetization measurements were performed. Figure 16 shows that the weak ferromagnetic moment of Tb_3OsO_7 completely disappears when the temperature is increased above ca 60 K. That is, the antiferromagnetic interactions at low temperatures have a weak ferromagnetic component.

Figure 17 depicts the temperature dependence of the reciprocal susceptibility of Tb_3OsO_7, and the Curie-Weiss fitting in the temperature range of 100 and 400 K. The effective magnetic moment of

Tb_3OsO_7 is determined to be 16.81 μ_B. Since the moment of Tb^{3+} is 9.7 μ_B, the effective magnetic moment of Os^{5+} is calculated to be 0.60 μ_B. The contribution of the Os^{5+} ions to the effective magnetic moment of Tb_3OsO_7 is small, which is found in some Os-containing compounds [17, 37-42].

The negative Weiss constant of Tb_3OsO_7 (θ = -12.4 K) indicates that the magnetic interaction observed at low temperatures is antiferromagnetic.

Magnetic properties of Ln_3OsO_7 are summarized in Table 2.

3.3. Structural phase transition

The results of the specific heat measurements show that Pr_3OsO_7 undergoes a structural phase transition at 130 K (see Fig. 10). DSC measurements for Tb_3OsO_7 show that the structural phase transition occurs at 580 K (see Fig. 7).

Most of the Ln_3MO_7 compounds crystallize in the orthorhombic phase with space group *Cmcm*. *M* = Ru and Os compounds undergo a structural phase transition from space group *Cmcm* to $P2_1nb$ with decreasing temperature [12, 18, 26, 31]. Iridium compounds Ln_3IrO_7 show a phase transition from the orthorhombic phase with space group *Cmcm* to a monoclinic phase with space group $P2_1/n$ [34]. On the other hand, Ln_3MoO_7 show a phase transition from space group *Pnma* to $P2_12_12_1$[25, 45]. A neodymium tantalate Nd_3TaO_7 undergoes a phase transition from space group *Cmcm* to $C222_1$ [20].

Figure 18 shows the variation of the structural phase transition temperatures for a series of Ln_3MO_7 compounds (*M* = Mo, Re, Os, Ir, Ru) against the ionic radius of Ln^{3+} in eight-coordination. These M^{5+} ions have a *d*-electron configuration ranging from d^1 to d^4, indicating that the Ln_3MO_7 compounds are magnetically active. For each of the five series of Ln_3MO_7 compounds, the structure transition

temperatures decrease with increasing the ionic radius of Ln^{3+}, i.e., it is clear that the structure transition of Ln_3MO_7 is clearly influenced by the size of the Ln^{3+} cation. As the transition temperature increases with decreasing the ionic radius of Ln^{3+}, the transition is stress-induced and it occurs with lattice contraction on cooling. Each transition temperature within a series is separated by approximately the same temperature interval except for the case of Ln_3MoO_7. The reason for this may be related to the difference in their high-temperature structures, that is, Ln_3MO_7 (*M* = Ru, Re, Os, Ir) compounds exist in the *Cmcm* structure, whereas Ln_3MoO_7 exists in the *Pnma* structure.

Summary

Ternary rare-earth osmates Ln_3OsO_7 (*Ln* = Pr, Tb) have been prepared from the reaction of mixtures of Pr_2O_3 (Tb_2O_3), Pr_6O_{11} (Tb_4O_7) and OsO_2, without using oxygen donor reactants. We found a phase transition at 130 K (*Ln* = Pr) and 580 K (*Ln* = Tb). Magnetic ordering was observed at 8 and 73 K for Pr_3OsO_7, and 8 and 60 K for Tb_3OsO_7. These compounds Pr_3OsO_7 and Tb_3OsO_7 are candidates to behave as one-dimensional from the magnetic point of view, and 73 and 60 K correspond to the one-dimensional correlations temperatures of the antiferromagnetic interactions that take place along the Os-O-Os chains being in these Pr and Tb compounds that can be closely correlated with the decreasing of bond angle from 157° to 149° in going from Pr to Tb compounds.

References

[1] H. J. Rossell, *J. Solid State Chem.*, **27**, 115-122 (1979).

[2] F. P. F. van Berkel and D. J. W. IJdo, *Mater. Res. Bull.*, **21**, 1103-1106 (1986).

[3] W. A. Groen, F. P. F. van Berkel, and D. J. W. IJdo, *Acta Crystallogr*. Sec. **C 43**, 2262-2264 (1986).

[4] A. Kahn-Harari, L. Mazerrolles, D. Michel, and F. Robert, *J. Solid State Chem.*, **116**, 103-106 (1995).

[5] P. Khalifah, R. W. Erwin , J. W. Lynn, Q. Huang, B. Batlogg, and R. J. Cava, *Phys. Rev.*, **B 60**, 9573-9578 (1999).

[6] F. Wiss, N. P. Raju, A. S. Wills, and J. E. Greedan, *Inter. J. Inorg. Mater.*, **2**, 53-59 (2000).

[7] B.P.Bontchev, A.J.Jacobson, M.M.Gospodinov, V. Skumryev, V. N. Popov, B. Lorenz, R. L. Meng, A. P. Litvinchuk, and M.N. Iliev, *Phys. Rev*. **B. 62**, 12235-12240 (2000).

[8] D. Harada and Y. Hinatsu, *J. Solid State Chem*., **158**, 245-253 (2001).

[9] D. Harada, Y. Hinatsu, and Y. Ishii, *J. Phys.: Condens. Matter*, **13**, 10825-10836 (2001).

[10] D. Harada and Y. Hinatsu, *J. Solid State Chem*., **164**, 163-168 (2002).

[11] R. Lam, F. Wiss, and J. E. Greedan, *J. Solid State Chem.* **167**, 182-187 (2002).

[12] W. R. Gemmill, M. D. Smith, and H-C, zur Loye, *Inorg. Chem*., **43**, 4254-4261 (2004).

[13] N. Ishizawa, K. Hiraga, D. du Boulay, H. Hibino, T. Ida, and S. Oishi, *Acta Cryst*., **E62**, i13-i16 (2006).

[14] G. Wltschek, H. Paulus, I. Svoboda, H. Ehrenberg, and H. Fuess, *J.Solid State Chem*. **125**, 1-4 (1996).

[15] R. Lam, T. Langet, and J. E. Greedan, *J. Solid State Chem.* **171**, 317-323 (2002).

[16] Y. Hinatsu, M. Wakeshima, N. Kawabuchi, and N. Taira, *J. Alloys Compd*., **374**, 79-83 (2004).

[17] J. R. Plaisier, R. J. Drost, and D. J. W. IJdo, *J. Solid State Chem.* **169**, 189-198 (2002).

[18] W. R. Gemmill, M. D. Smith, Y. A. Mozharivsky, G. J. Miller, and H-C, zur Loye, *Inorg. Chem.*, **44**,

7047-7055 (2005).

[19] J. F. Vente, R. B. Helmholdt, and D. J. W. IJdo, *J. Solid State Chem*. **108**, 18-23 (1994).

[20] M. Wakeshima, H. Nishimine, and Y. Hinatsu, *J. Phys.: Condens. Matter*, **16**, 4103-4120 (2004).

[21] J. F. Vente and D. J. W. IJdo, *Mater. Res. Bull.*, **26**, 1255-1262 (1991).

[22] H. Nishimine, M. Wakeshima, and Y. Hinatsu, *J. Solid State Chem*., **177**, 739-744 (2004).

[23] J. E. Greedan, N. P. Raju, A. Wegner, P. Gougeon, and J. Padiou, *J. Solid State Chem*., **129**, 320-327 (1997).

[24] N. Barrier and P. Gougeon, *Acta Crystallogr.*, **E59**, i22-i24 (2003).

[25] H. Nishimine, M. Wakeshima, and Y. Hinatsu, *J. Solid State Chem*., **178**, 1221-1229 (2005).

[26] N. Ishizawa, K. Tateishi, S. Kondo, and T. Suwa, *Acta Crystalllogr*., **47**, 558-566 (2006).

[27] N. Barrier, P. Gall, and P. Gougeon, *Acta Crystallogr*., **C63**, i102-i104 (2007).

[28] W. R. Gemmill, M. D. Smith, and H-C, zur Loye, *J. Chem*. Crystallogr, **37**, 793-795 (2007).

[29] N. Ishizawa, T. Suwa, K. Tateishi, and J. R. Hester, *Acta Crystalllogr*., **C63**, i43-i46 (2007).

[30] N. Ishizawa, T. Suwa, and K. Tateishi, *Acta Crystalllogr*., **E63**, i163 (2007).

[31] N. Ishizawa, K. Tateishi, S. Kondo, and T. Suwa, *Inorg. Chem.*, **47**, 558-566 (2008).

[32] Y. Doi, Y. Harada, and Y. Hinatsu, *J. Solid State Chem.*, **182**, 709-715 (2009).

[33] Y. Hinatsu, H. Ebisawa, and Y. Doi, *J. Solid State Chem.*, **182**, 1694-1699 (2009).

[34] Y. Hinatsu, Y. Doi, H. Nishimine, M. Wakeshima, and M. Sato, *J. Alloys Compd*., **488**, 541-545 (2009).

[35] F. Izumi and K. Momma, *Solid State Phenom.*, **130**, 15-20 (2007).

[36] K. Momma and F. Izumi, *Appl. Crystallogr*., **41**, 653-658 (2008).

[37] F. Abraham, J. Trehoux, and D. Thomas, *J. Inorg. Nucl. Chem.*, **42**, 1627-1630 (1980).

[38] K. E. Stitzer, A. ElAbed, M. D. Smith, M. J. Davis, S-J. Kim, J. Darriet, and H-C. zur Loye, *Inorg. Chem.*, **42**, 947-949 (2003).

[39] L. Chi, I. P. Swainson, and J. E. Greedan, *J. Solid State Chem.*, **177**, 3086-3091 (2004).

[40] K. E. Stitzer, M. D. Smith, H-C. zur Loye, *Solid State Sciences*, **4**, 311-316 (2002).

[41] W. R. Gemmill, M. D. Smith, R. Prozorov, and H-C. zur Loye, *Inorg. Chem.*, **44**, 2639-2646 (2005).

[42] K. Yamamura, M. Wakeshima, and Y. Hinatsu, *J. Solid State Chem.*, **179**, 605-612 (2006).

[43] B. C. Gerstein, F. J. Jelinek, and F. H. Spedding, *Phys. Rev. Lett.* **8**, 425 (1962).

[44] J. B. Mac Chesney, H. J. Williams, R. C. Sherwood, and J. F. Potter, *J. Chem. Phys.*, **44**, 596 (1966).

[45] M. Wakeshima and Y. Hinatsu, *J. Solid State Chem.*, **183**, 2681-2688 (2010).

Figure captions

Fig. 1 (a) Powder X-ray diffraction profile for Pr_3OsO_7 at room temperature. The calculated and observed profiles are shown on the top solid line and cross markers, respectively. The vertical marks in the middle show positions calculated for Bragg reflections. The lower trace is a plot of the difference between calculated and observed intensities.

(b) Powder X-ray diffraction profile for Tb_3OsO_7 at room temperature. The calculated profiles based on the *Cmcm* model are shown on the top solid line. The vertical marks in the middle show positions calculated for Bragg reflections. The lower trace is a plot of the difference between calculated and observed intensities. Arrows show the diffraction lines which cannot be indexed with *Cmcm* (see text).

Fig. 2 Crystal structure of Pr_3OsO_7 (space group: *Cmcm*).

Fig. 3 X-ray diffraction profiles of Tb_3OsO_7 at various temperatures. Arrows show the diffraction lines which cannot be indexed with *Cmcm* (see text).

Fig. 4 Powder X-ray diffraction profile for Tb_3OsO_7 measured at 673 K. The calculated and observed profiles are shown on the top solid line and cross markers, respectively. The vertical marks in the middle show positions calculated for Bragg reflections. The second vertical marks show positions for impurities $Tb_2Os_2O_7$. The lower trace is a plot of the difference between calculated and observed intensities.

Fig. 5 Powder X-ray diffraction profile for Tb_3OsO_7 at room temperature. The calculated and observed profiles are shown on the top solid line and cross markers, respectively. The vertical marks in the middle show positions calculated for Bragg reflections. The second vertical marks show

positions for impurities $Tb_2Os_2O_7$. The lower trace is a plot of the difference between calculated and observed intensities.

Fig. 6 Crystal structure of Tb_3OsO_7 at room temperature (space group: $P2_1nb$).

Fig. 7 DSC profile of Tb_3OsO_7 during heating in the temperature range between 350 and 700 K. An arrow shows the temperature at which the endothermic reaction begins.

Fig. 8 Temperature dependence of lattice parameters and volume for Tb_3OsO_7 in the temperature range between 373 and 723 K.

Fig. 9 Temperature dependence of the magnetic susceptibility for Pr_3OsO_7 in the temperature range of 1.8 and 300 K. The inset shows the temperature dependence of the $d(\chi_M T)/dT$ at low temperatures.

Fig.10 Temperature dependence of the specific heat divided by temperature (C_p/T) for Pr_3OsO_7.

Fig.11 Temperature dependence of the reciprocal magnetic susceptibility for Pr_3OsO_7. The solid line is the Curie-Weiss fitting.

Fig.12 Temperature dependence of the magnetic susceptibility for Tb_3OsO_7.

Fig.13 Temperature dependence of the in-phase and the out-of-phase ac magnetic susceptibility for Tb_3OsO_7 in the temperature range of 1.8 and 100 K. The applied magnetic field is 0.0005 T with frequencies of 10 ~ 10,000 Hz.

Fig.14 Temperature dependence of the specific heat for Tb_3OsO_7 in the temperature range between 1.8 and 100 K. The inset shows the detailed temperature dependence of the specific heat below 30 K.

Fig.15 Field dependence of the magnetization for Tb_3OsO_7 measured at 5, 20, and 50K.

Fig.16 Temperature dependence of the remnant magnetization for Tb_3OsO_7.

Fig.17 Temperature dependence of the reciprocal magnetic susceptibility for Tb_3OsO_7. The solid line is the Curie-Weiss fitting.

Fig.18 Structural phase transition temperatures of Ln_3MO_7 (M = Mo, Ru, Re, Os, Ir) against the ionic radius of Ln^{3+} in eight-coordination.

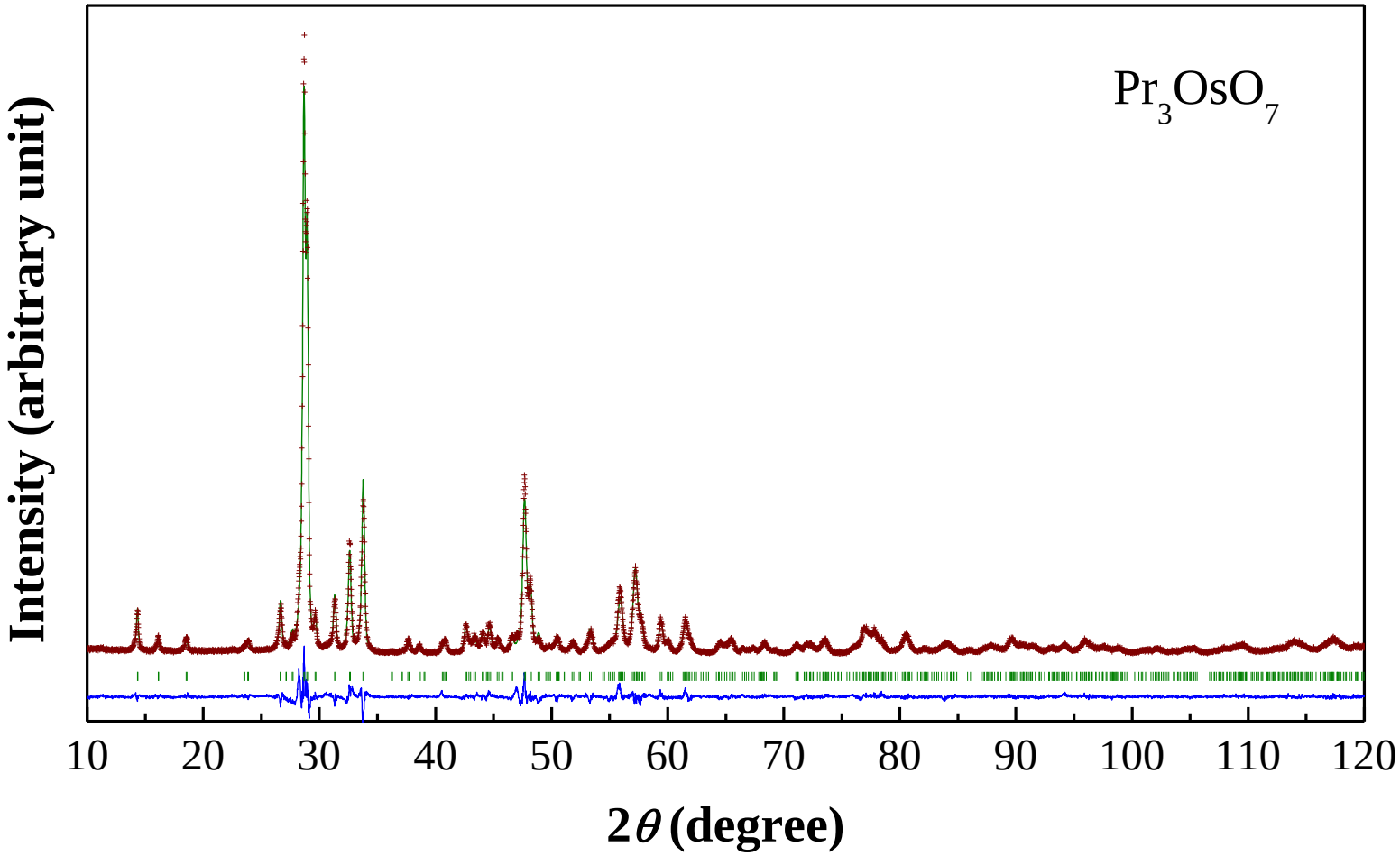

Pr3OsO7
Intensity (arbitrary unit)
10
20
30
40
50
60
70
80
90
100
110
120
2θ (degree)

Fig.1(a)

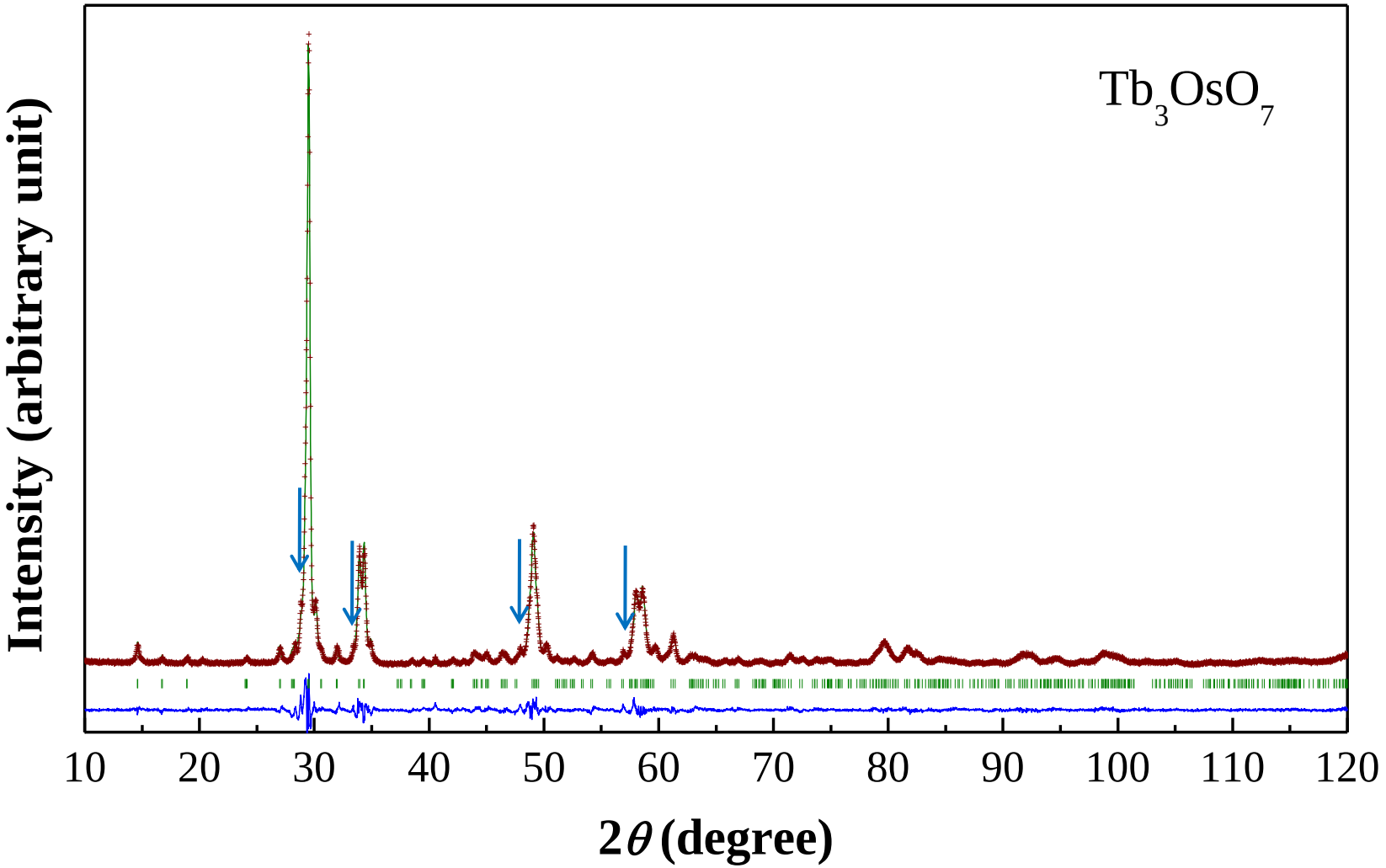

Tb3OsO7
Intensity (arbitrary unit)
10
20
30
40
50
60
70
80
90
100
110
120
2θ (degree)

Fig. 1(b)

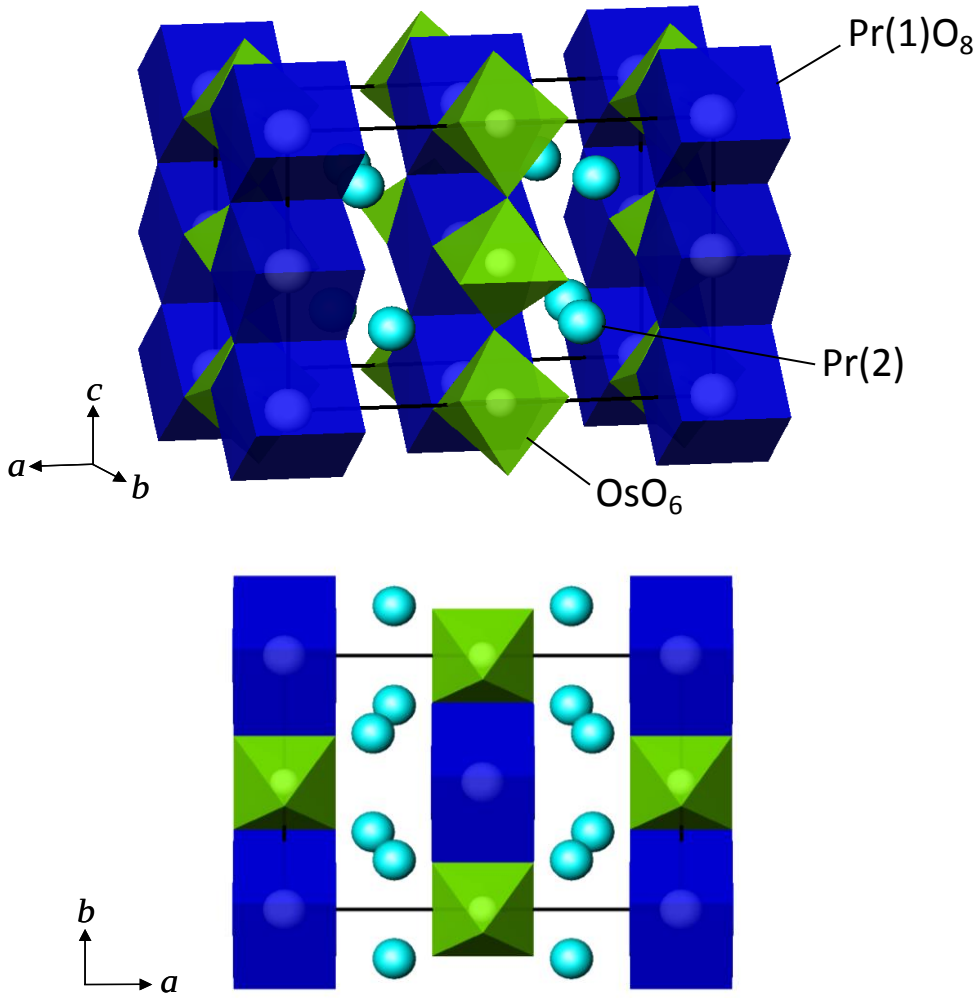


Fig. 2

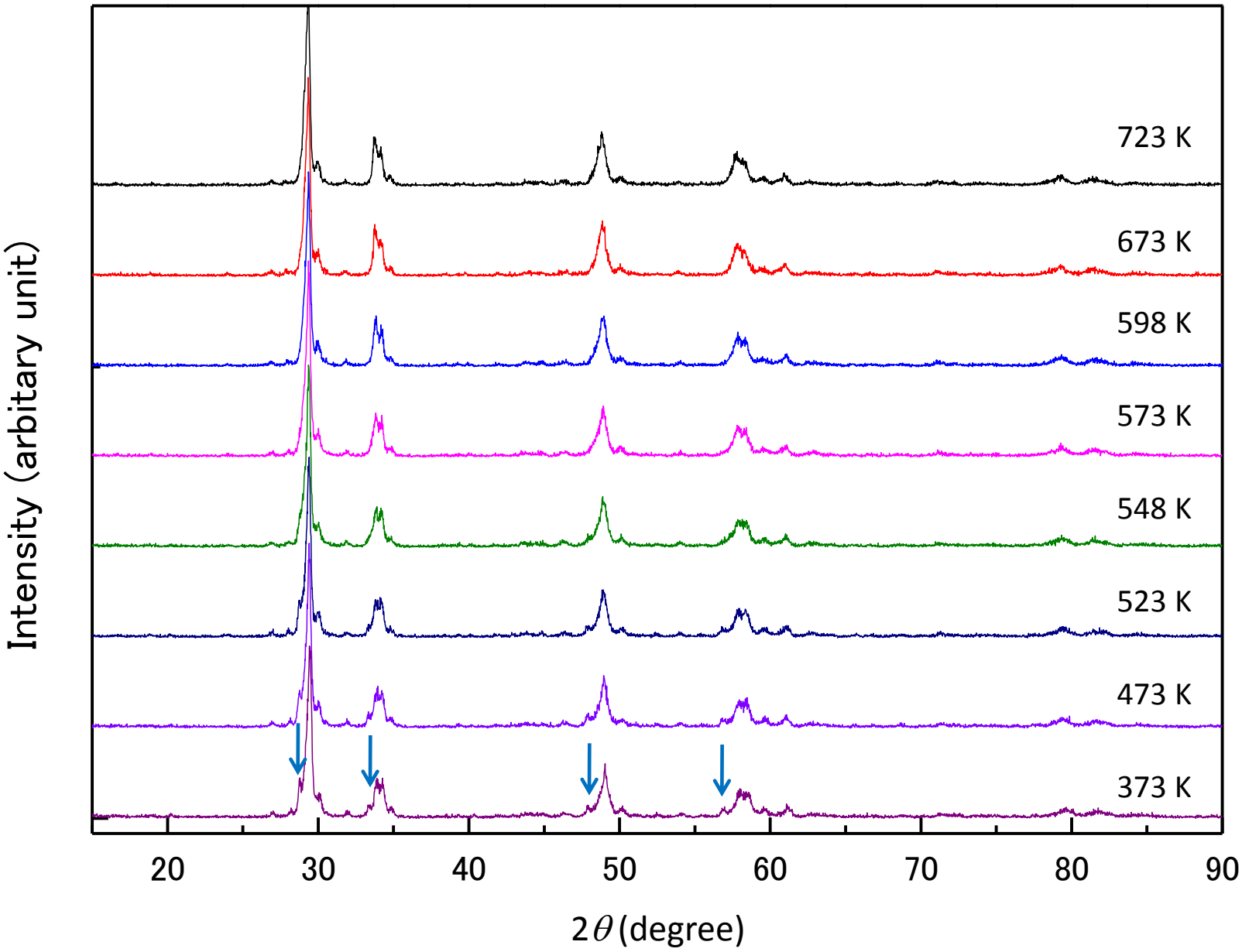

723 K
673 K
598 K
573 K
548 K
523 K
473 K
373 K
Intensity (arbitary unit)
20
30
40
50
60
70
80
90
2θ (degree)

Fig.3

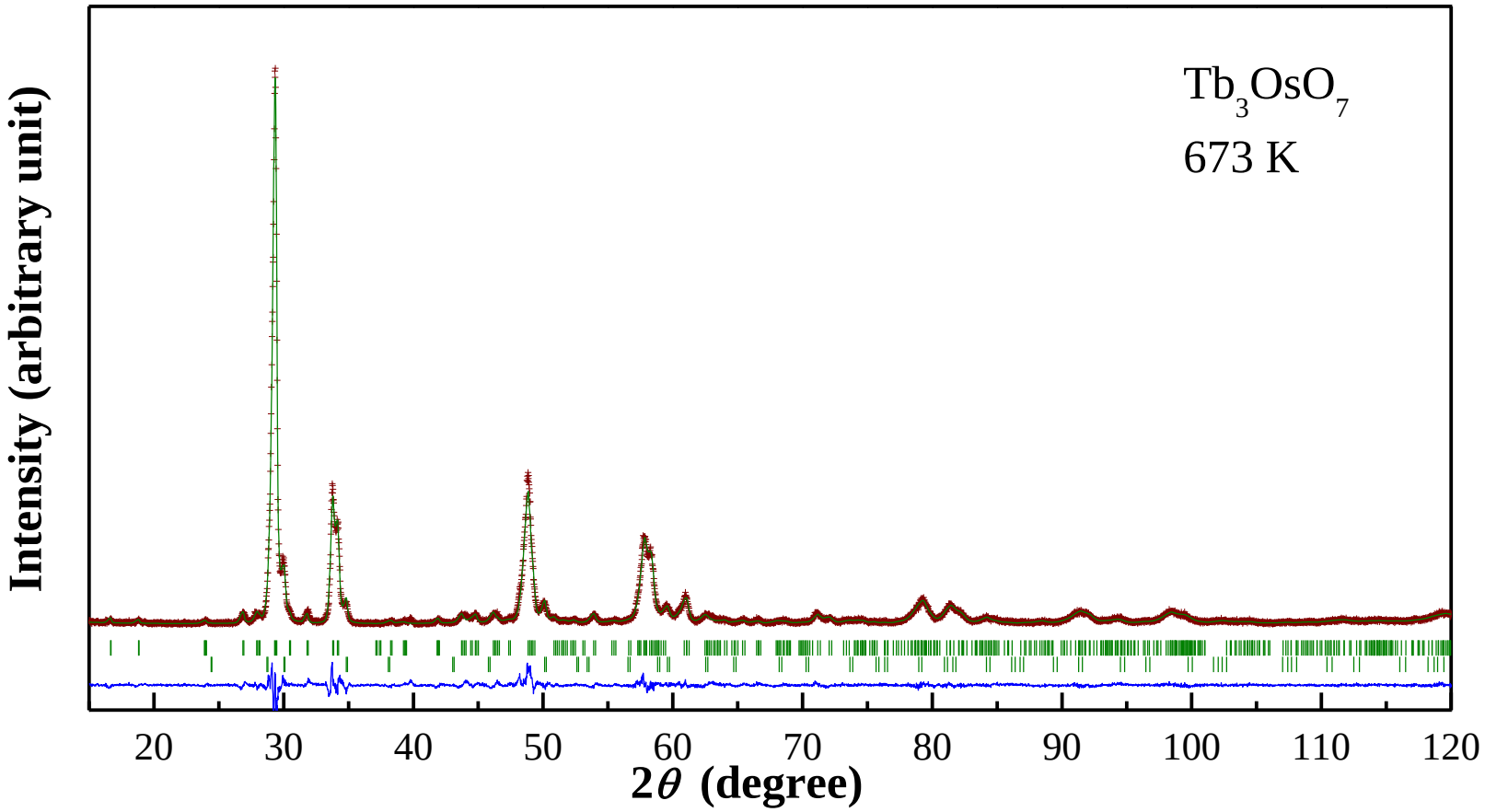

Tb3OsO7
673 K
Intensity (arbitrary unit)
20
30
40
50
60
70
80
90
100
110
120
2θ (degree)

Fig.4

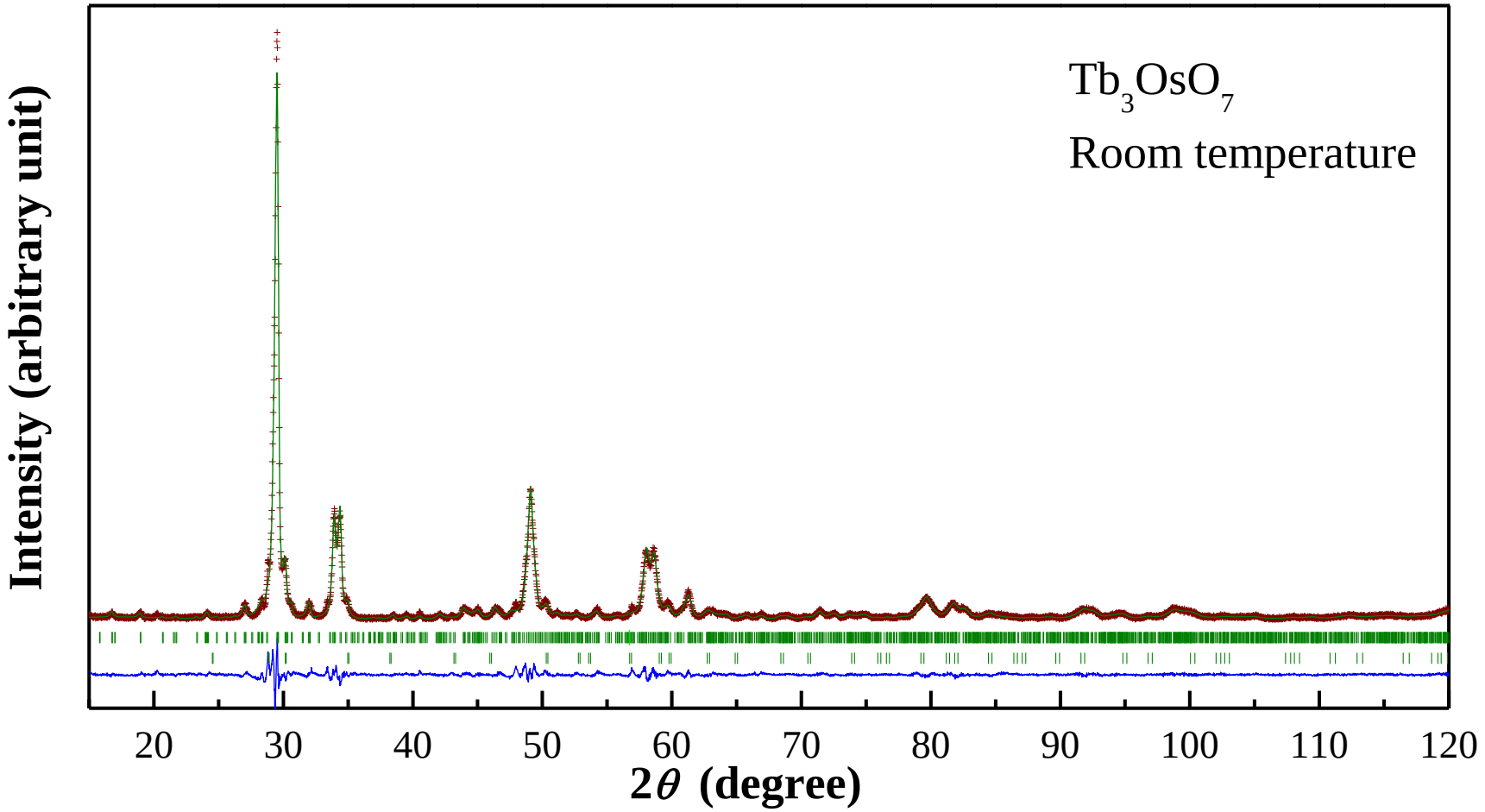
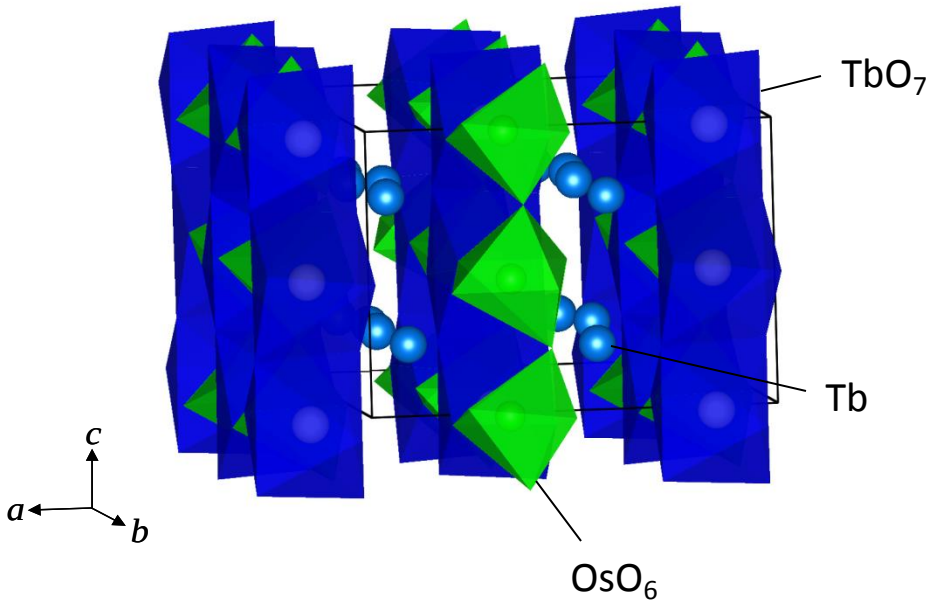

Tb3OsO7
Room temperature
Intensity (arbitrary unit)
20
30
40
50
60
70
80
90
100
110
120
2θ (degree)

Fig.5



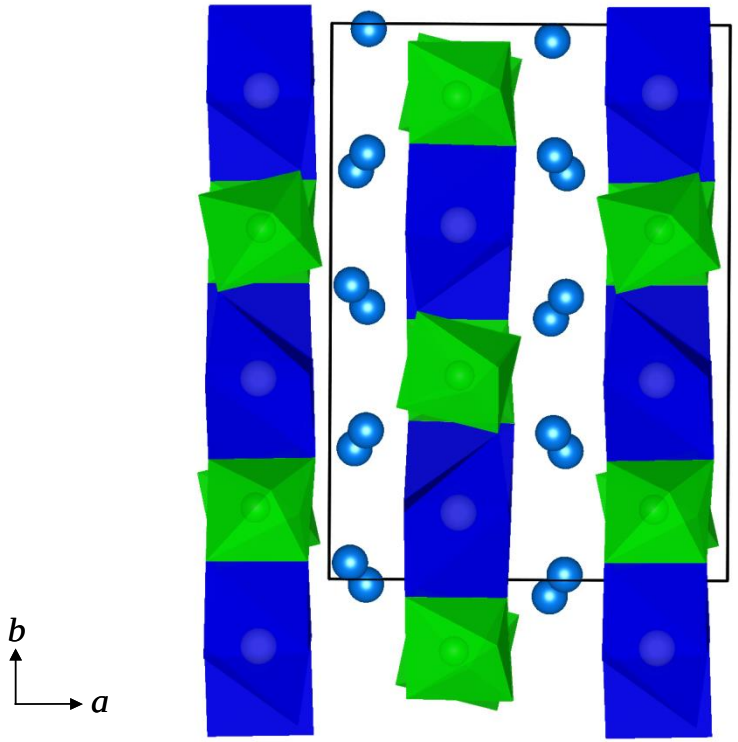


Fig.6

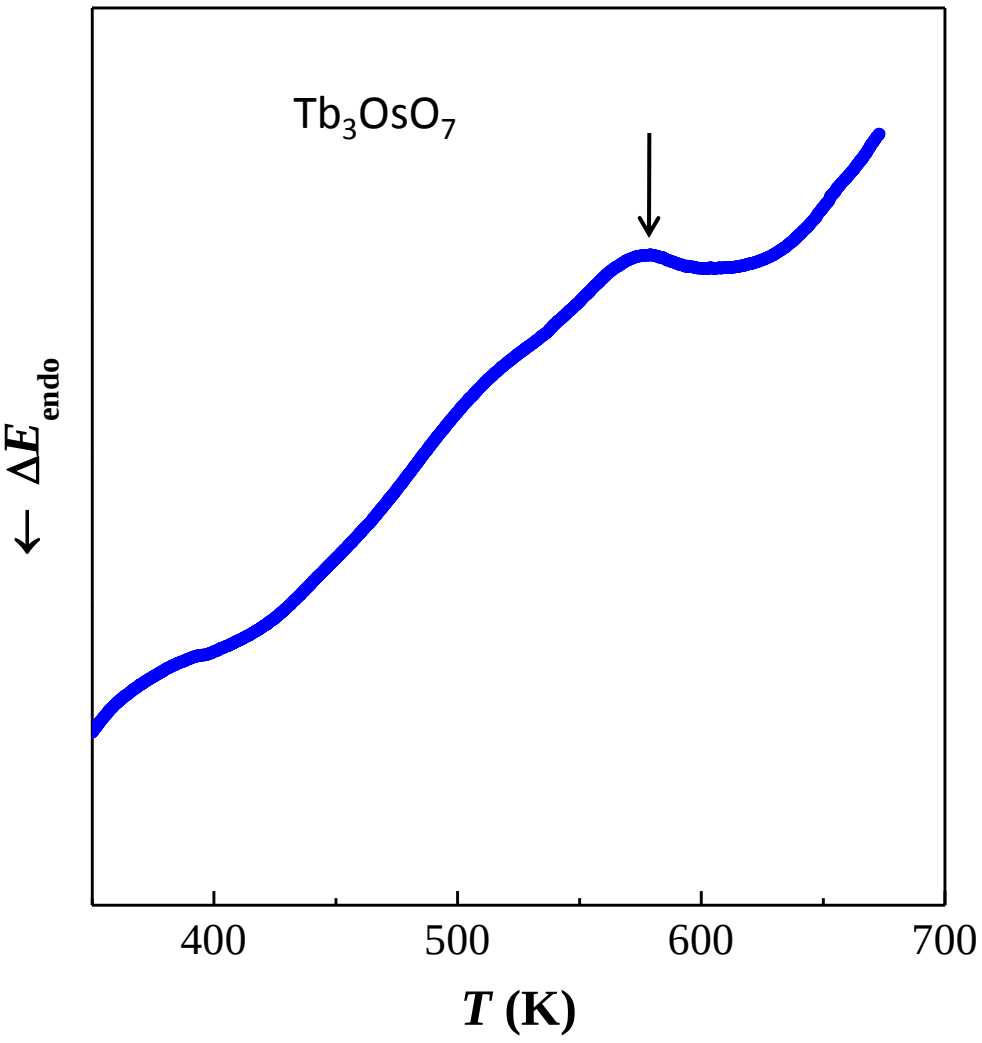


Fig.7

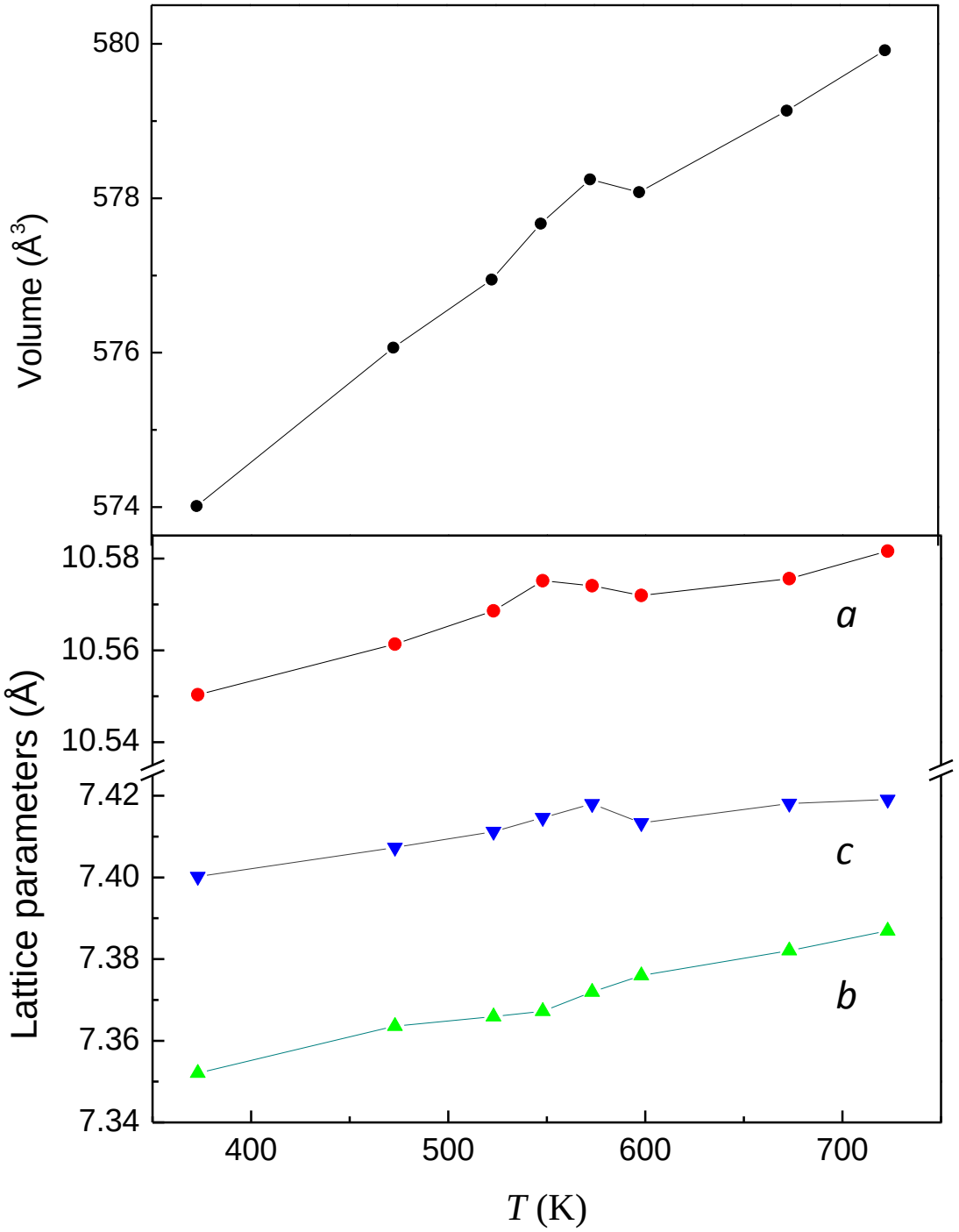

580
578
576
574
Volume (Å^3)
10.58
10.56
10.54
7.42
7.40
7.38
7.36
7.34
Lattice parameters (Å)
a
c
b
400
500
600
700
T (K)

Fig.8

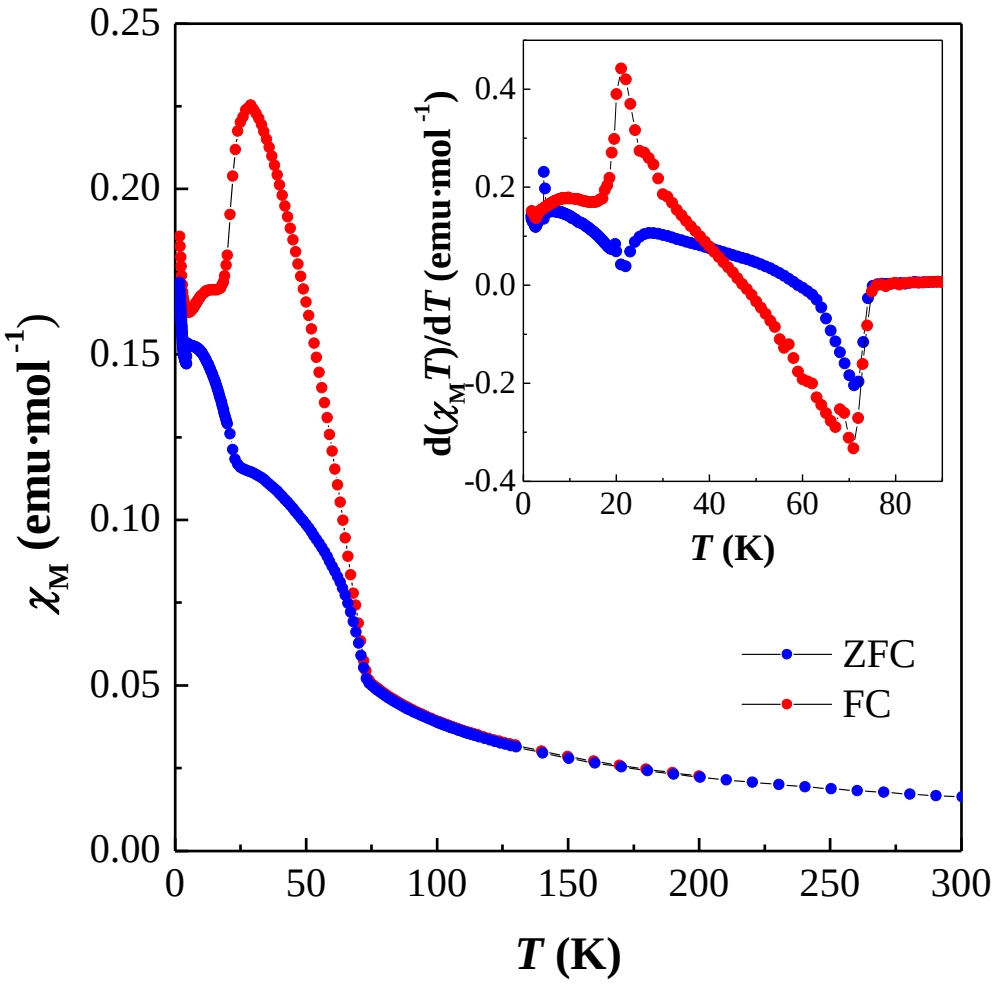

0.25
0.20
0.15
0.10
0.05
0.00
0
50
100
150
200
250
300
χ_M (emu·mol^{-1})
T (K)
ZFC
FC
0.4
0.2
0.0
-0.2
-0.4
0
20
40
60
80
d($\chi_M T$)/dT (emu·mol^{-1})
T (K)

Fig. 9

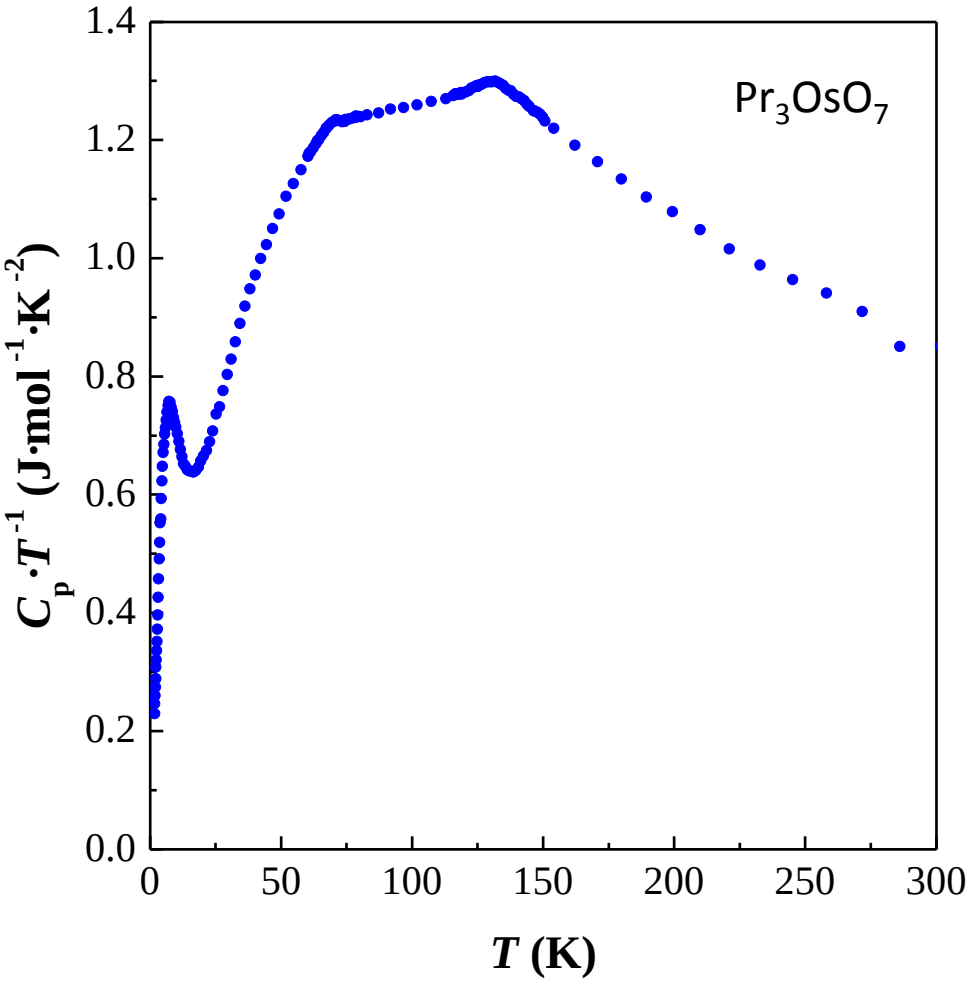

1.4
1.2
1.0
0.8
0.6
0.4
0.2
0.0
0
50
100
150
200
250
300
$C_p \cdot T^{-1}$ (J·mol^{-1}·K^{-2})
T (K)
Pr_3OsO_7

Fig.10

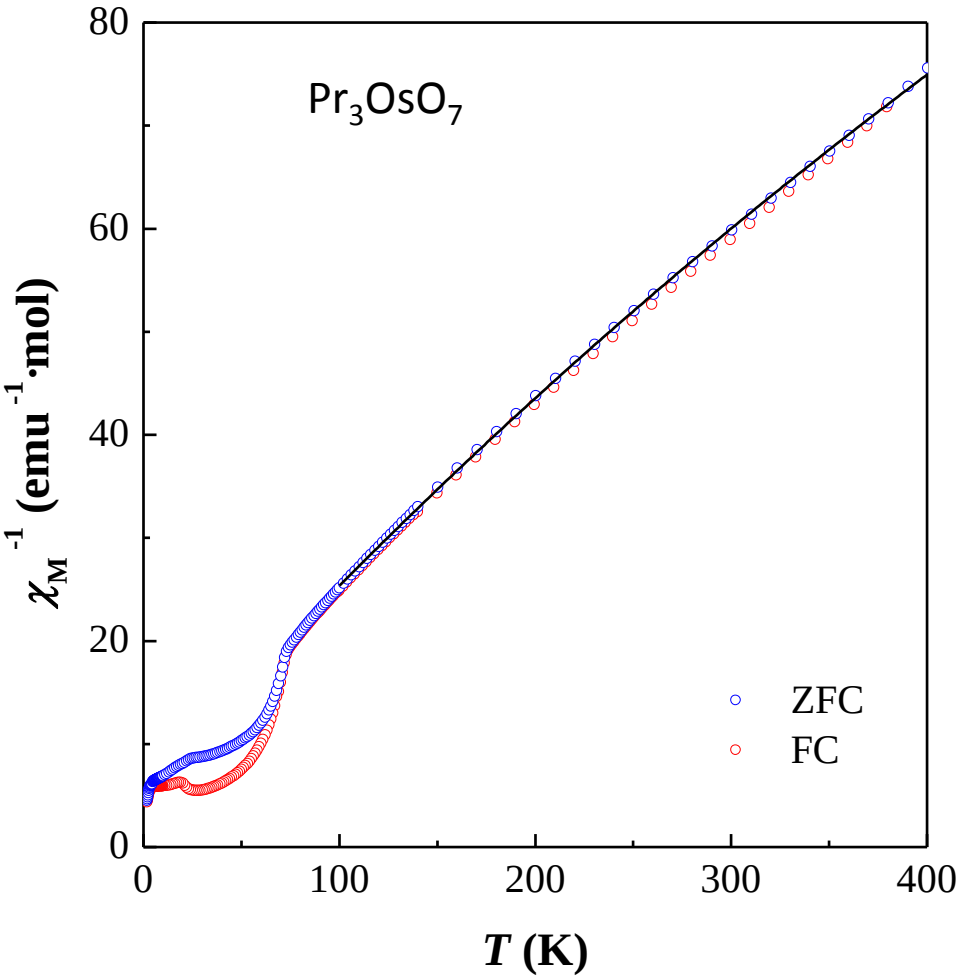


Fig.11

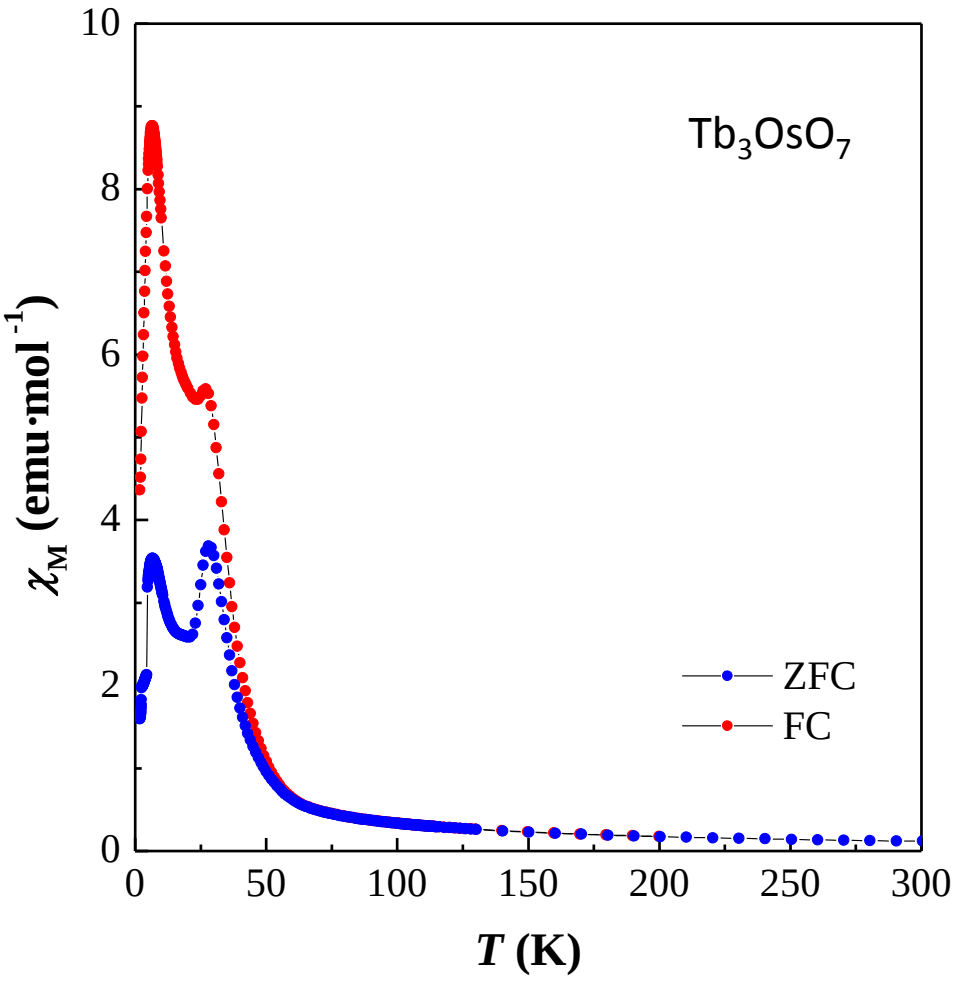

10
8
6
4
2
0
0
50
100
150
200
250
300
χ_M (emu·mol^{-1})
T (K)
Tb_3OsO_7
ZFC
FC

Fig. 12

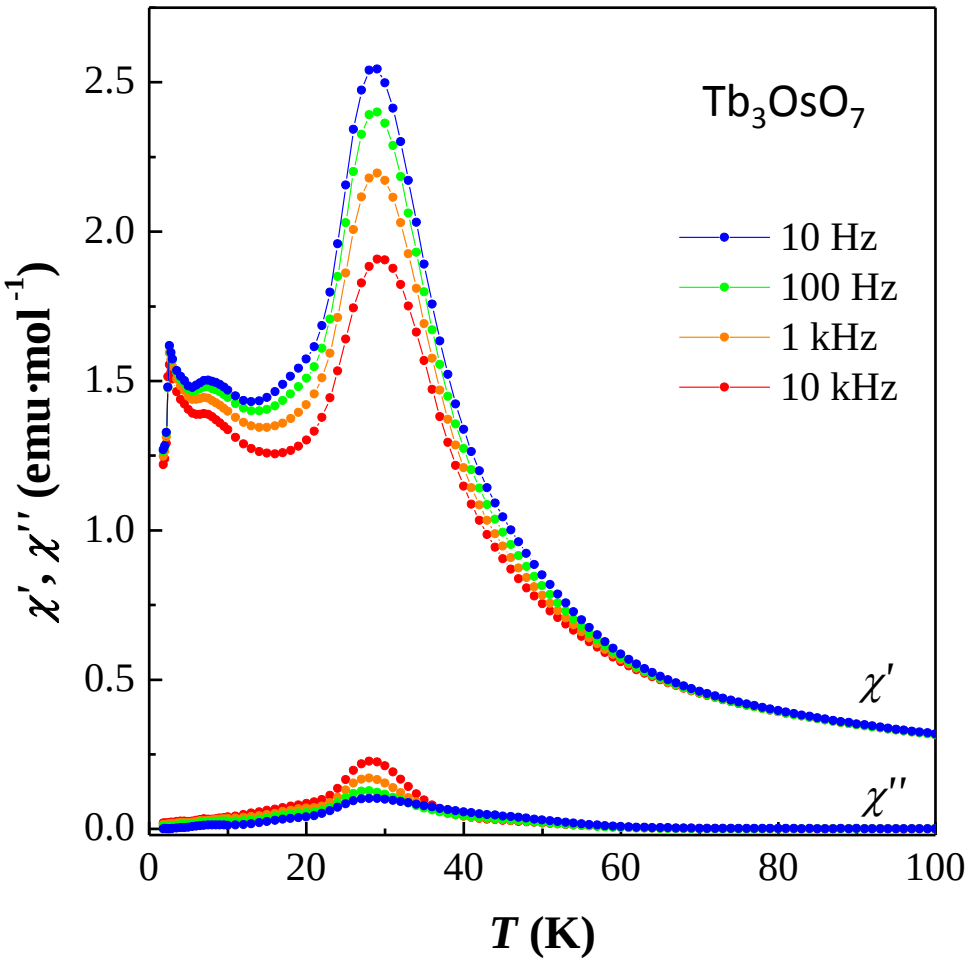

Tb3OsO7
10 Hz
100 Hz
1 kHz
10 kHz
χ'
χ''
χ', χ'' (emu·mol-1)
T (K)
0.0
0.5
1.0
1.5
2.0
2.5
0
20
40
60
80
100

Fig.13

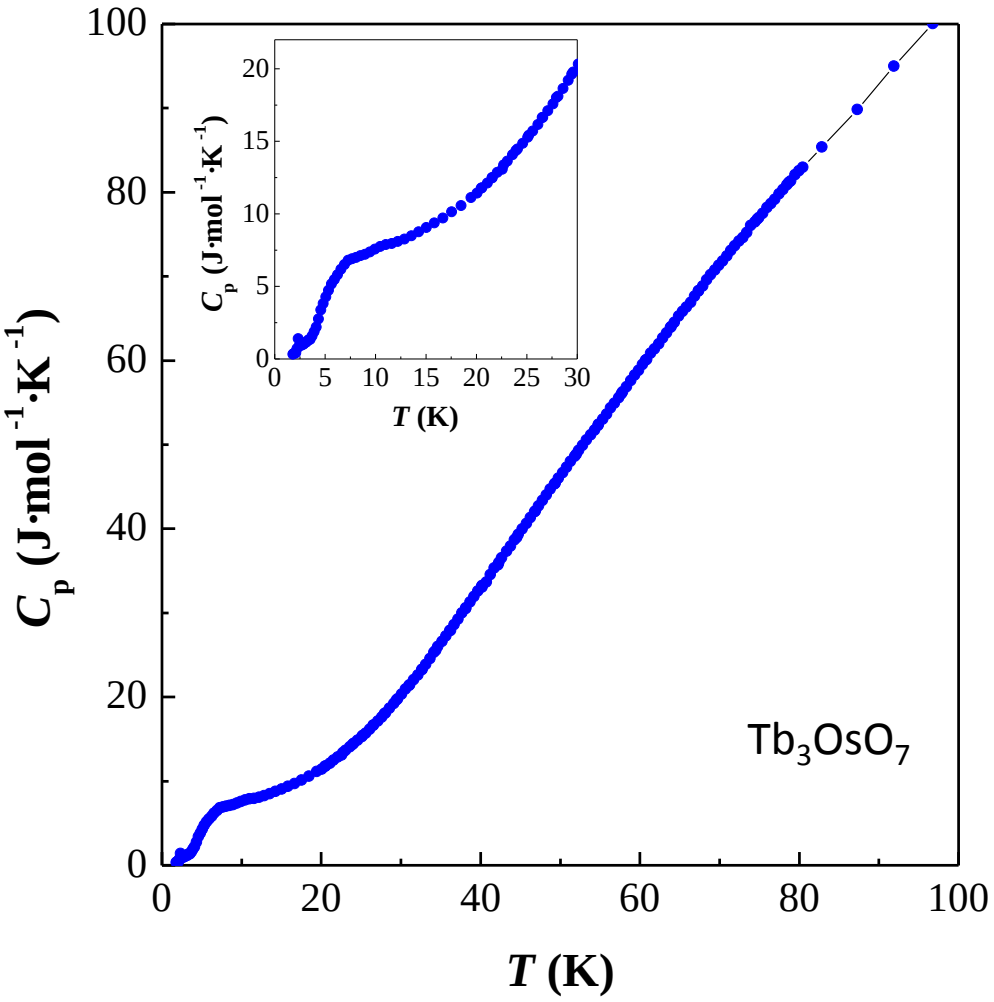

100
80
60
40
20
0
0
20
40
60
80
100
C_p (J·mol^{-1}·K^{-1})
T (K)
Tb_3OsO_7
20
15
10
5
0
0
5
10
15
20
25
30
C_p (J·mol^{-1}·K^{-1})
T (K)

Fig.14

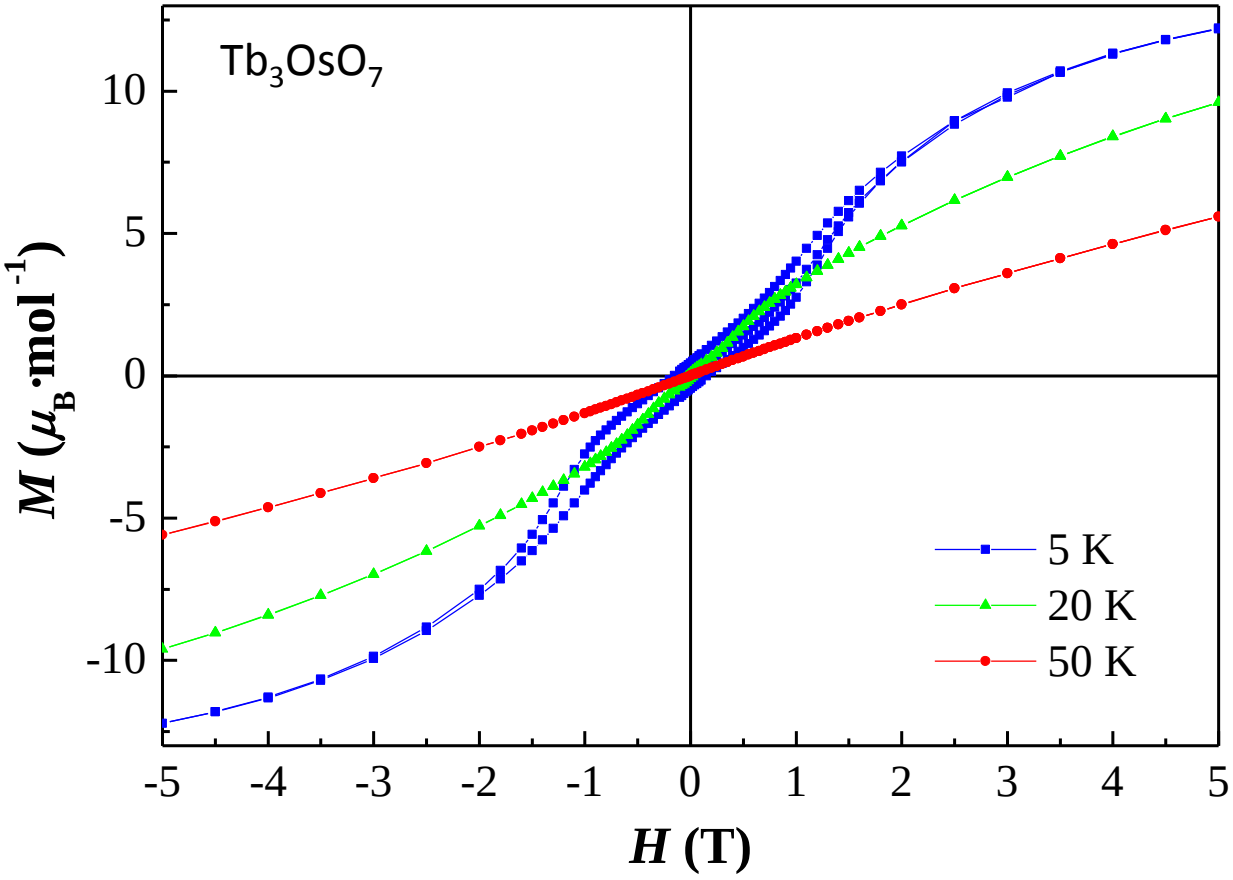


Fig.15

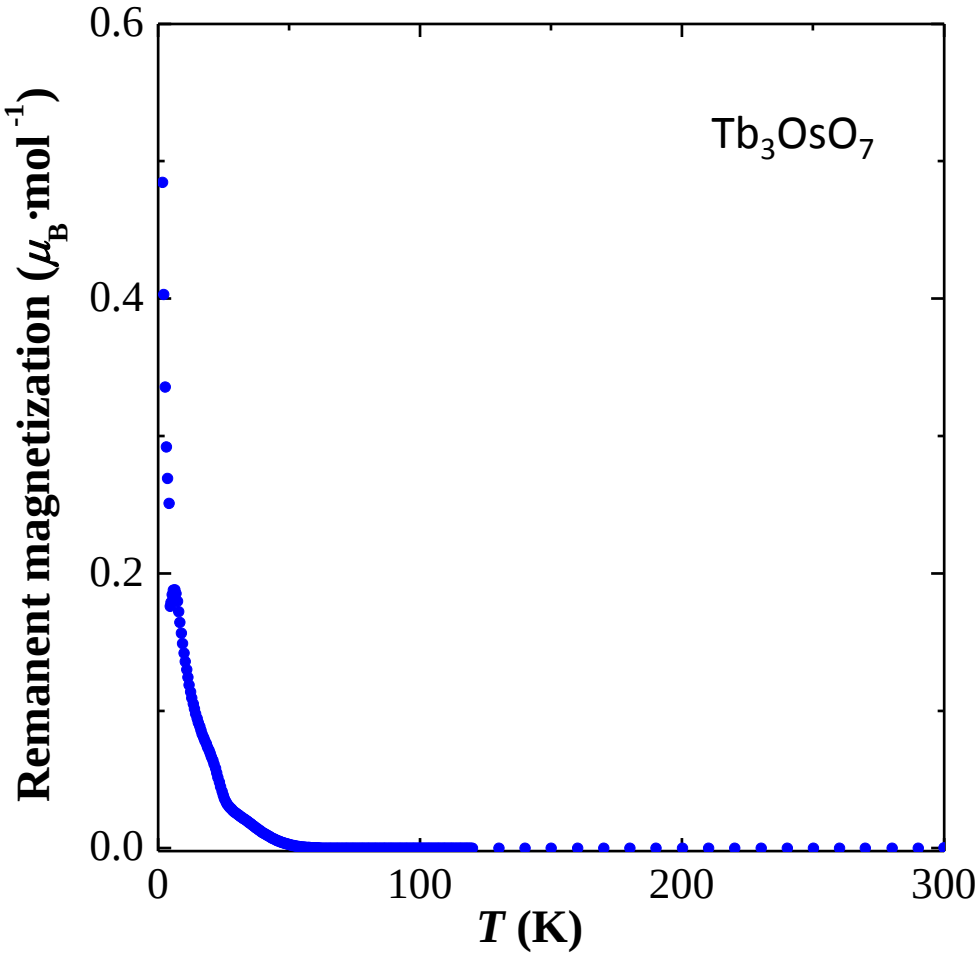

Tb3OsO7
Remanent magnetization (μB·mol-1)
T (K)
0.0
0.2
0.4
0.6
0
100
200
300

Fig.16

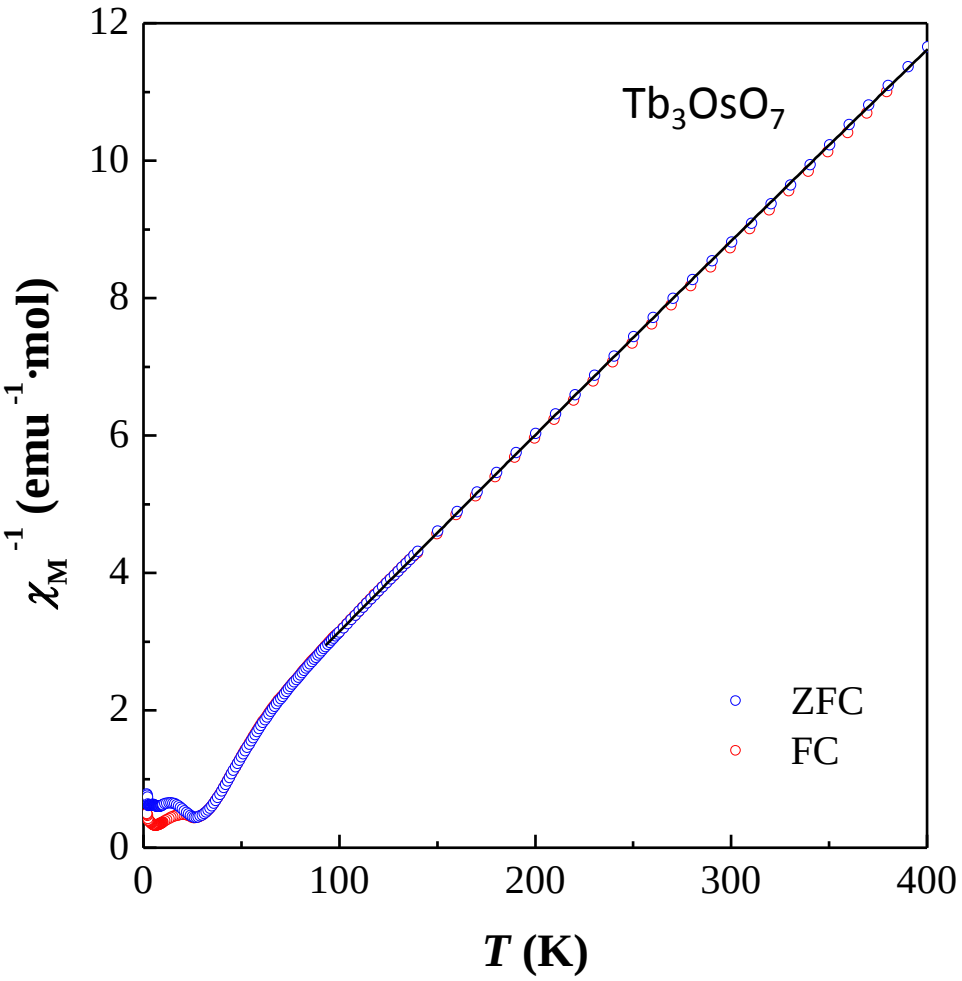


Fig.17

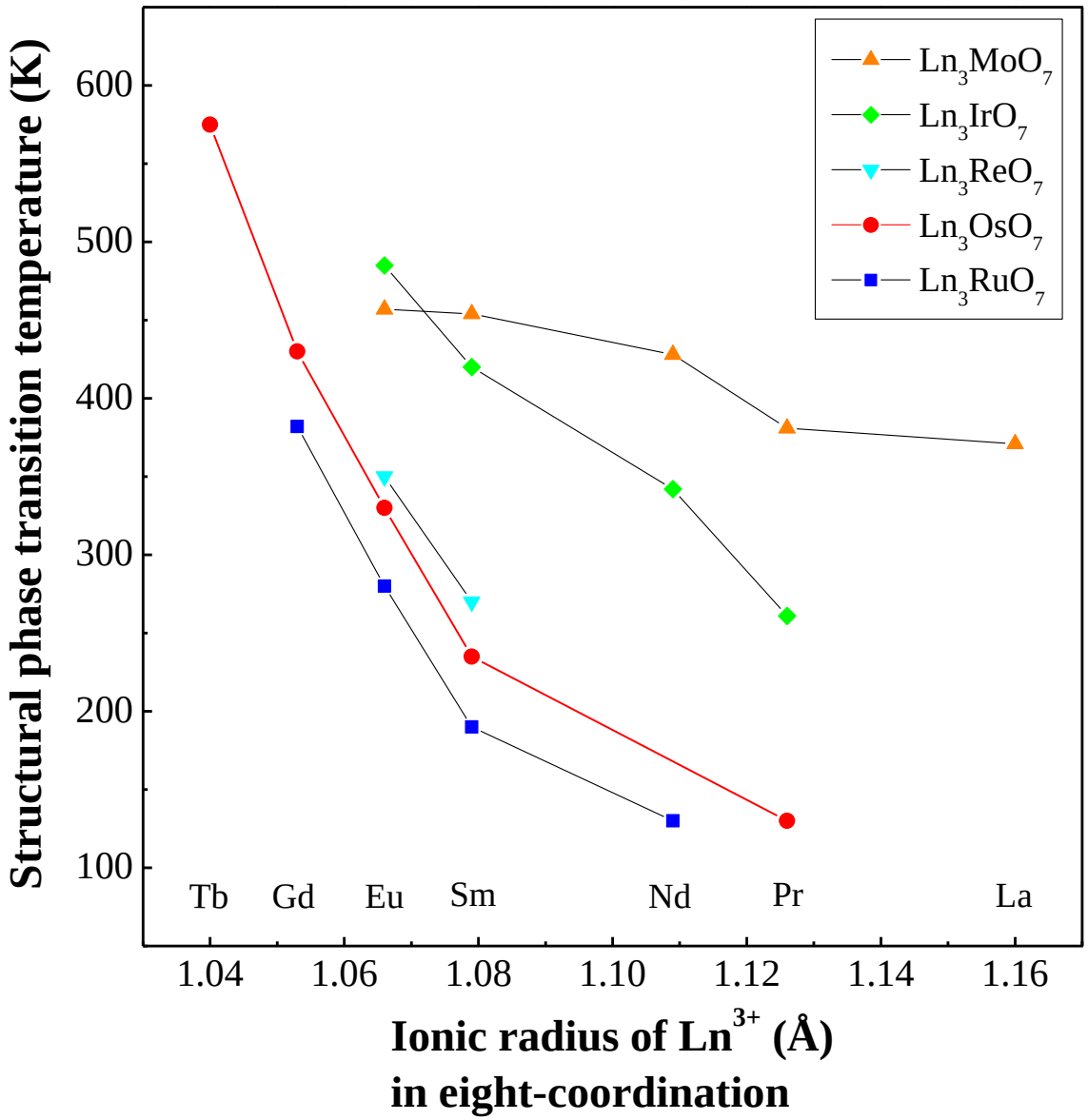

Structural phase transition temperature (K)
600
500
400
300
200
100
Tb
Gd
Eu
Sm
Nd
Pr
La
1.04
1.06
1.08
1.10
1.12
1.14
1.16
Ionic radius of Ln3+ (Å)
in eight-coordination
Ln3MoO7
Ln3IrO7
Ln3ReO7
Ln3OsO7
Ln3RuO7

Fig.18

Table 1 Structural parameters for Ln_3OsO_7 (*Ln* = Pr, Tb).

Pr_3OsO_7 at room temperature

Atom	Site	*x*	*y*	*z*	*B* / Å^2 [a]
Pr(1)	4*a*	0	0	0	0.89(7)
Pr(2)	8*g*	0.2259(1)	0.3054(2)	1/4	0.57(5)
Os	4*b*	0	1/2	0	0.41(6)
O(1)	16*h*	0.126(1)	0.314 (1)	–0.042(1)	1.2(2)
O(2)	8*g*	0.135(1)	0.032(1)	1/4	1.2
O(3)	4*c*	0	0.448(2)	1/4	1.2

Note. Space group *Cmcm*; a = 10.9732(15) Å, b = 7.4485(10) Å, c = 7.5507(10) Å, V = 617.15(14) Å^3, R_{wp} = 11.59 %, R_B = 1.84 %, and R_e = 7.48 %, where $R_{wp} = \left[\sum_i w_i \left(y_i - f_i(\boldsymbol{x})\right)^2 / \sum_i w_i {y_i}^2 \right]^{1/2}$, $R_B = \sum_K \left| I_O(\boldsymbol{h}_K) - I(\boldsymbol{h}_K) \right| / \sum_K I_O(\boldsymbol{h}_K)$, and $R_e = \left[(N-P) / \sum_i w_i {y_i}^2 \right]^{1/2}$.

Tb_3OsO_7 at 673 K

Atom	Site	*x*	*y*	*z*	*B* / Å^2 [a]
Tb(1)	4*a*	0	0	0	1.15(9)
Tb(2)	8*g*	0.2351(1)	0.2796(2)	1/4	0.77(6)
Os	4*b*	0	1/2	0	0.21(6)
O(1)	16*h*	0.135(1)	0.295 (1)	–0.033(2)	1.7(3)
O(2)	8*g*	0.137(3)	0.017(3)	1/4	1.7
O(3)	4*c*	0	0.431(4)	1/4	1.7

Note. Space group *Cmcm*; a = 10.5771(9) Å, b = 7.3842(7) Å, c = 7.4164(9) Å, V = 579.28(10) Å^3, R_{wp} = 11.54 %, R_B = 1.75 %, and R_e = 7.98 %.

Table 2 Magnetic data for Ln_3OsO_7

compounds	magnetic properties	μ_{eff} (μ_B)	θ (K)	Ref.
La_3OsO_7	T_N = 45K, 110K, non Curie-Weiss behavior up to 500 K	3.93	-278	[11]
Pr_3OsO_7	T_N = 8, 73 K	6.37	-39.9	this study
Nd_3OsO_7	T_C = 75 K	6.89	~0	[17]
Sm_3OsO_7	Weak ferromagnetic, T_C = 48 K	4.19	-8	[17]
Eu_3OsO_7	Complex behavior below 50 K	*	*	[18]
Gd_3OsO_7	Ferromagnetic, T_C = 34 K	13.7	1.6	[18]
Tb_3OsO_7	T_N = 8, 60 K	16.81	-12.4	this study

* These values are not shown in the reference.